

DRAFT CMS Paper

The content of this note is intended for CMS internal use and distribution only

2023/01/27

Archive Hash: f251f4e-D

Archive Date: 2023/01/27

Search for long-lived particles decaying in the CMS muon detectors in proton-proton collisions at $\sqrt{s} = 13$ TeV

The CMS Collaboration

Abstract

A search for long-lived particles (LLPs) produced in decays of standard model (SM) Higgs bosons is presented. The data sample consists of 137 fb^{-1} of proton-proton collisions at $\sqrt{s} = 13$ TeV, recorded at the LHC in 2016–2018. A novel technique is employed to reconstruct decays of LLPs in the muon detectors. The search is sensitive to a broad range of LLP decay modes and to masses below 1 GeV. No excess of events above the SM background is observed. The most stringent limits to date on the branching fraction of the Higgs boson to LLPs subsequently decaying to quarks and $\tau^+\tau^-$ are found for proper decay lengths greater than

This box is only visible in draft mode. Please make sure the values below make sense.

PDFAuthor: C. Pena, C. Wang
PDFTitle: Search for neutral long-lived particles decaying in the CMS muon system
PDFSubject: CMS
PDFKeywords: CMS, your topics

Please also verify that the abstract does not use any user defined symbols

1 Introduction

Many extensions of the standard model (SM) predict the existence of neutral, weakly-coupled particles that have long proper lifetimes. These long-lived particles (LLPs) naturally arise in models of split supersymmetry (SUSY) [1–6], SUSY with weak R -parity violation [7–10], SUSY with gauge-mediated supersymmetry breaking [11–13], stealth SUSY [14, 15], hidden valley scenarios [16–18], baryogenesis triggered by weakly interacting massive particles [19–21], inelastic dark matter [22], and Twin Higgs models [23–25].

In this paper, we describe a search at the CERN Large Hadron Collider (LHC) that uses muon detectors as sampling calorimeter to identify showers produced by decays of LLPs. The search is based on proton-proton (pp) collision data at 13 TeV collected during 2016–2018 at the LHC, corresponding to an integrated luminosity of 137 fb^{-1} . The CMS muon detectors are composed of detector planes interleaved with the steel layers of the magnet flux-return yoke. Decays of LLPs in the muon detectors induce hadronic and electromagnetic showers, giving rise to a high hit multiplicity in localized detector regions. The hadron calorimeter, solenoid magnet, and steel flux-return yoke together provide 12–27 nuclear interaction lengths of shielding, which is sufficiently large to suppress particle showers that are not fully contained (punch-through) to negligible levels.

This search has sensitivity to singly or multiply produced LLPs decaying to final states including hadrons, taus, electrons, or photons. The LLPs decaying to muons will very rarely produce a particle shower and will remain undetected by this search. While this search is sensitive to many models predicting LLPs, we interpret the result in two separate benchmark models. The first model that we focus on is a benchmark simplified model motivated by the twin Higgs scenario [16–18, 26–28] where the SM Higgs boson (H) decays to a pair of neutral long-lived scalars (S), each of which decays in turn to a pair of fermions. Further details of the simplified model can be found in Ref. [29]. The most stringent previous limit for mean proper decay lengths $c\tau < 0.3 \text{ m}$ is based on a search for displaced jets in the CMS tracker [29]. For $c\tau > 0.3 \text{ m}$, displaced vertices in the ATLAS muon spectrometer [30, 31] and the previous iteration of this analysis using the CMS endcap muon detectors [32] set the most stringent previous limit. The second model that we interpret the search result in is the hidden valley model with perturbative parton showers that could span a wide range of dark shower phenomenology. We consider production through the SM Higgs boson (H) that decays to a pair of dark sector quarks, each of which hadronize into a dark shower consisting of prompt and long-lived dark sector mesons that eventually decay back to Standard Model particles. Depending on the symmetries and decay portal, the proper lifetime of the dark mesons and the final state SM particles can vary, resulting a wide range of dark shower phenomenology. We interpret the search result in the 5 decay portals presented in Ref. [33], including the gluon portal producing hadron-rich showers, photon portal with photon showers, vector portal with semi-visible jets, Higgs portal with heavy flavor-rich showers, and dark photon portal with lepton-rich showers. The Feynman diagrams of the two benchmark models are shown in Figure 1.

There are two inherent advantages of using the CMS muon detectors as a sampling calorimeter to detect LLPs over past searches that employ displaced vertices: (i) the absorber material in front of the muon detectors acts as a shield to maintain a sufficiently low level of background with the detection of a single LLP decay, a level that current displaced vertex searches can only achieve by requiring the detection of two LLP decays; (ii) the calorimetric nature of the particle shower, sensitive to the LLP energy rather than its mass, renders this search equally sensitive to all LLP masses considered, while vertex reconstruction efficiency tends to decrease with the LLP mass due to increasingly smaller opening angles.

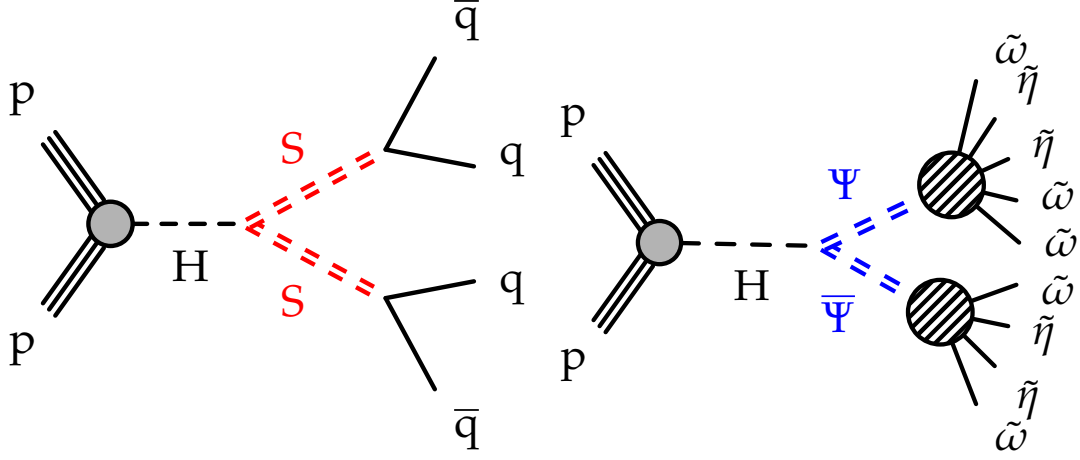


Figure 1: Feynman diagrams of Twin Higgs model (left) and dark shower model (right). In the Twin Higgs model (left), the SM Higgs boson (H) decays to a pair of neutral long-lived scalars (S), which then decays to two SM particles (q). In the dark shower model, the SM Higgs boson (H) decays to a pair of dark sector quarks (Ψ), which then hadronizes to form dark showers consisting of dark mesons ($\tilde{\omega}$ and $\tilde{\eta}$) that decay back to SM particles.

Because of these advantages, the signal acceptance and sensitivity are improved relative to the previous best results [30–32] for all LLP masses and proper lifetimes. The improved categorization of splitting events with single or double LLPs result from reaching improved Higgs boson to LLP decay branching fractions to below 10^{-4} , in addition to keeping the advantage of large signal acceptance at very large $c\tau$.

The rest of this paper is organized as follows. We briefly describe the CMS detector in Section 2. Section 3 provides a summary of the simulated samples used in the analysis. The reconstruction of the muon detector shower clusters are detailed in Section 4 and the event selections are described in Section 5. The background estimation methods are detailed in Section 6. The signal modelling and systematic uncertainties are discussed in Sections 7 and 8, respectively. We report and interpret the results in Section 9. Finally, a summary is given in Section 10. The tabulated results and instructions to reproduce the signal efficiency are provided in HEPData [34].

2 The CMS detector

The central feature of the CMS apparatus is a superconducting solenoid of 6 m internal diameter, providing a magnetic field of 3.8 T. Within the solenoid volume are a silicon pixel and strip tracker, a lead tungstate crystal electromagnetic calorimeter (ECAL), and a brass and scintillator hadron calorimeter (HCAL), each composed of a barrel and two endcap sections. Forward calorimeters extend the pseudorapidity coverage provided by the barrel and endcap detectors. Muons are detected in detectors embedded in the steel flux-return yoke outside the solenoid using three technologies: drift tubes (DTs) in the barrel, cathode strip chambers (CSCs) in the endcaps, and resistive-plate chambers (RPCs) in the barrel and endcaps. A more detailed description of the CMS detector, together with a definition of the coordinate system used and the relevant kinematic variables, can be found in Ref. [35].

The DT and CSC detectors covering the barrel and endcaps, respectively, play critical roles for the search described in this paper.

The barrel DT detectors cover a region of pseudorapidity $|\eta| < 1.2$ and are organized into 4 stations of concentric cylinders around the beamline, labeled MB1 to MB4, which are located approximately 4, 5, 6, and 7 m away from the interaction point radially (r), interleaved between the layers of the steel flux-return yoke. As charged particles traverse the DT stations that contain 8–12 layers of drift tube cells, they will ionize the gas molecules and produce charges that drift to the anode wire at the center of the DT cells. A signal pulse at the anode wire is measured as a hit. At the hit level, since there is ambiguity about the direction of the drift, all hits are assumed to be at the center of the DT cells. The first 3 stations each contain 12 layers of drift tube cells, in 3 groups of 4 staggered layers called “superlayers” (SL). The innermost and outermost SLs measure the hit coordinate in the $r\phi$ -plane, and the central SL measures in the z direction, along the beamline. The fourth station only contains two SLs measuring the hit position in the $r\phi$ -plane.

The CSC detector covers a region of pseudorapidity between $|\eta| = 0.9$ and 2.4 and is composed of four “stations” in each endcap, labeled ME1 to ME4, which are located approximately 7, 8, 9.5, and 10.5 m away from the interaction point along the beamline axis (z) on both ends of the detector, and are sandwiched between steel absorbers. Each chamber is composed of six thin layers containing cathode strips along the radial direction and anode wires perpendicular to the strips. Charged particles traversing the chambers ionize the gas molecules. The resulting electrons are accelerated towards the anode wires producing an avalanche, while the positive ions travel to the opposite end and induce signals in the cathode strips. By combining the information from signals on the anode wires and the cathode strips of each layer, we can determine the space-time coordinates of each such “hit” with a resolution of 400–500 μm and 5 ns [36].

Events of interest are selected using a two-tiered trigger system. The first level, composed of custom hardware processors, uses information from the calorimeters and muon detectors to select events at a rate of around 100 kHz within a fixed latency of about 4 μs [37]. The second level, known as the high-level trigger, consists of a farm of processors running a version of the full event reconstruction software optimized for fast processing, and reduces the event rate to around 1 kHz before data storage [38].

3 Simulated samples

The simulated $h^0 \rightarrow \text{SS}$ signal samples are generated using POWHEG 2.0 [39–42], and include gluon fusion, vector boson fusion, WH, ZH, and $t\bar{t}H$ production modes. The Higgs boson

mass is set to 125 GeV, while the S mass (m_S) is set to 0.4, 1, 3, 7, 15, 40, or 55 GeV. The $c\tau$ is varied between 1 mm and 100 m. We also consider various decay modes, including fully hadronic decays, to $b\bar{b}$, $d\bar{d}$, K^+K^- , $K^0\bar{K}^0$, and $\pi^+\pi^-$, fully leptonic decays to $\pi^0\pi^0$, $\gamma\gamma$, e^+e^- , and decays to $\tau^+\tau^-$.

For the simulated hidden valley signal samples, the Higgs production is generated using POWHEG 2.0 [39–42] and includes only gluon fusion mode. The Higgs boson mass is set to 125 GeV. Higgs decaying to dark sector quarks and phenomenology of the dark showers are generated following the tools and theory priors presented in Ref. [33], using the PYTHIA 8 hidden valley module [43–45]. As mentioned in Section 1, we generate signal samples of 5 different decay portals. For each decay portal, the LLP mass is varied between 2 - 20 GeV. The minimum LLP mass considered depends on the theoretically motivated minima discussed in Ref. [33]. The $c\tau$ is varied between 1 mm and 10 m. Finally, we consider three sets of numerical values for $x_{i\omega}$, the mass ratio of the dark vector meson ($\tilde{\omega}$) to the dark scalar meson ($\tilde{\eta}$), and $x_{i\Lambda}$, the ratio of the dark scalar meson mass to the dark sector QCD scale: $(x_{i\omega}, x_{i\Lambda}) = (2.5, 2.5), (2.5, 1), (1, 1)$. These three scenarios present a wide range of phenomenology with different LLP multiplicity, multiplicity of visible decays, and missing energy.

For both signal models, parton showering, hadronization, and the underlying event are modeled by PYTHIA 8.205 and 8.230 [45] with parameters set by the CUETP8M1 [46] and CP5 tunes [47] used for samples simulating the 2016 and 2017/18 datasets respectively.

The NNPDF 3.0 [48] and 3.1 [49] parton distribution functions are used in the generation of all simulated samples. The GEANT4 [50] package is used to model the response of the CMS detector, and simulated minimum-bias events are mixed with the hard interactions in simulated events to match the observed pileup distribution in data.

4 Muon Detector Showers

For LLPs that decay within or just prior to the muon system, the material in the iron return yoke structure will induce a hadronic or electromagnetic shower, creating a geometrically localized and isolated cluster of signal hits in the muon detectors.

When charge particles traverse the CSC chambers, signal pulses are collected on the anode wires and the cathode strips. The signals from wire groups are combined with signals from the cathode strips to form a two-dimensional point on each chamber layer called a CSC hit. When charge particles traverse the DT chambers, signal pulses are collected on the anode wires at the center of the DT cells and 1-dimensional point that are positioned at the center of each DT cells called DT hits are formed.

Since the CSC and DT hits contain different information, the CSC and DT hits are handled separately. The CSC and DT hits are clustered in η and the azimuthal angle ϕ (in radians) using the DBSCAN algorithm [51], which groups hits by high-density regions. A minimum of 50 hits and a “distance parameter” of 0.2 is used. We then merge two clusters that are nearby if the ΔR between two clusters is < 0.6 , until all clusters within an event are isolated. This merging procedure ensures that clusters coming from the same source are reconstructed as one object. In the overlap region of the muon detectors, with pseudorapidity $0.9 < |\eta| < 1.2$, if both CSC and DT clusters are reconstructed with $\Delta R < 0.4$, the CSC clusters are given precedence and DT clusters are removed.

The cluster reconstruction efficiency strongly depends on the LLP decay position. The efficiency is highest when the LLP decays near the edge of the shielding absorber material, where

there is enough material to induce the shower, but not so much that it stops the shower secondaries.

The cluster reconstruction efficiency (both DT and CSC clusters) is shown as a function of the simulated r and z decay positions of the particle S in Fig 2. The cluster reconstruction efficiencies for DT and CSC are shown separately as a function of the simulated r (z) decay positions of the particle S for DT (CSC) clusters in Fig 3. A p_T^{miss} selection of > 200 GeV is applied to the plots to ensure that the cluster efficiencies shown are relevant to the signal region of the search.

The cluster efficiency also depends on whether the LLP decays hadronically or leptonically. In general, hadronic showers have higher efficiency, since they are more likely to penetrate through the steel in between stations, while showers induced from electromagnetic decays generally occupy just one station and are stopped by the steel between stations. Overall, the CSC cluster efficiency is approximately 80% for fully hadronic decays, 55% for $\tau^+\tau^-$ decays, and 35% for fully leptonic decays. The DT cluster efficiency is approximately 80% for fully hadronic decays, 60% for $\tau^+\tau^-$ decays, and 45% for fully leptonic decays.

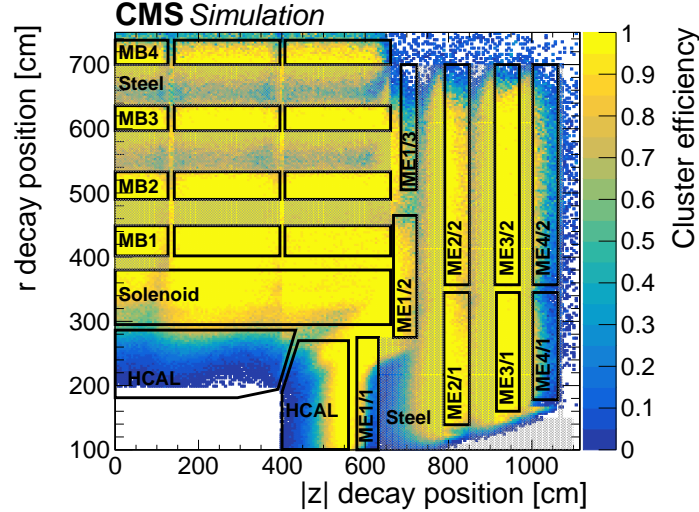


Figure 2: The cluster reconstruction efficiency (including both DT and CSC clusters) as a function of the simulated r and z decay positions of S decaying to $d\bar{d}$, for a mass of 40 GeV and a uniform mixture of $c\tau$ between 1 and 10 m. The barrel and endcap muon stations are drawn as black boxes and labeled by their station names. Regions occupied by steel shielding are shaded in gray.

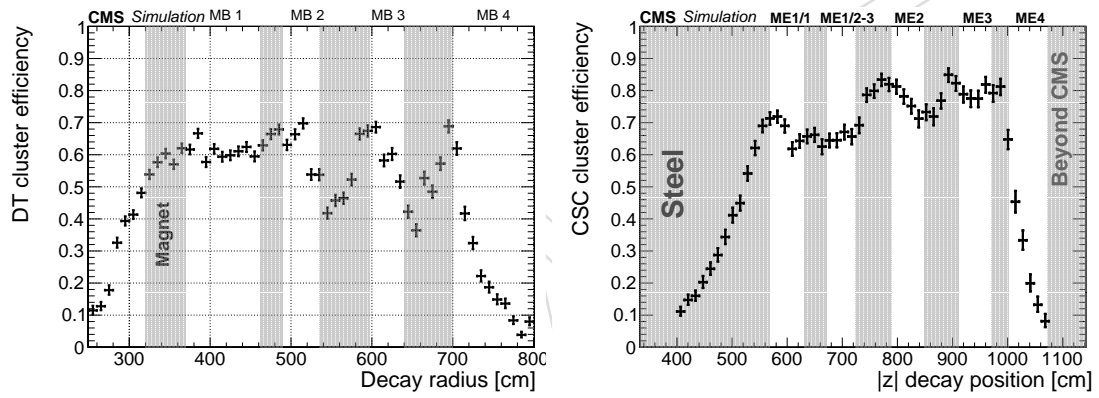


Figure 3: The DT (left) and CSC (right) cluster reconstruction efficiency as a function of the simulated r or z decay positions of S decaying to $d\bar{d}$, for a mass of 40 GeV and a uniform mixture of $c\tau$ between 1 and 10 m. Regions occupied by steel shielding are shaded in gray.

5 Search strategy and event selection

The particle-flow algorithm [52] aims to reconstruct and identify each individual particle in an event, with an optimized combination of information from the various elements of the CMS detector. The energy of photons is obtained from the ECAL measurement. The energy of electrons is determined from a combination of the electron momentum at the primary interaction vertex as determined by the tracker, the energy of the corresponding ECAL cluster, and the energy sum of all bremsstrahlung photons spatially compatible with originating from the electron track. The energy of muons is obtained from the curvature of the corresponding track. The energy of charged hadrons is determined from a combination of their momentum measured in the tracker and the matching ECAL and HCAL energy deposits, corrected for the response function of the calorimeters to hadronic showers. Finally, the energy of neutral hadrons is obtained from the corresponding corrected ECAL and HCAL energies.

For each event, hadronic jets are clustered from these reconstructed particles using the infrared and collinear safe anti- k_T algorithm [53, 54] with a distance parameter of 0.4. Jet momentum is determined as the vectorial sum of all particle momenta in the jet, and is found from simulation to be, on average, within 5 to 10% of the true momentum over the whole p_T spectrum and detector acceptance. Additional proton-proton interactions within the same or nearby bunch crossings (pileup) can contribute additional tracks and calorimetric energy depositions to the jet momentum. To mitigate this effect, charged particles identified to be originating from pileup vertices are discarded and an offset correction is applied to correct for remaining contributions. Jet energy corrections are derived from simulation to bring the measured response of jets to that of particle level jets on average. In situ measurements of the momentum balance in dijet, photon + jet, Z + jet, and multijet events are used to account for any residual differences in the jet energy scale between data and simulation [55]. The jet energy resolution amounts typically to 15–20% at 30 GeV, 10% at 100 GeV, and 5% at 1 TeV [55]. Additional selection criteria are applied to each jet to remove jets potentially dominated by anomalous contributions from various subdetector components or reconstruction failures.

The missing transverse momentum vector \vec{p}_T^{miss} is computed as the negative vector sum of the transverse momenta of all the PF candidates in an event, and its magnitude is denoted as p_T^{miss} [56]. The \vec{p}_T^{miss} is modified to account for corrections to the energy scale of the reconstructed jets in the event.

An LLP that decays after it has traversed the calorimeter systems can produce large p_T^{miss} because its momentum will remain undetected, as p_T^{miss} is calculated solely from the tracker and calorimeter information. We exploit this feature by triggering on events with $p_T^{\text{miss}} > 120$ GeV [57], and subsequently requiring offline $p_T^{\text{miss}} > 200$ GeV. We require at least one jet with $p_T > 30$ GeV and pseudorapidity $|\eta| < 2.4$, because signal events passing the p_T^{miss} requirement are always produced together with a jet from initial-state radiation. In addition, to suppress noncollision backgrounds, we apply filters that remove events containing beam-halo muons or calorimeter noise [58]. The event-level selections are kept minimal to be as model independent as possible.

After the event-level p_T^{miss} selection, the analysis is separated to 3 mutually exclusive categories based on the number and location of the clusters: 1) events with two clusters in the muon detectors, 2) events with exactly one CSC cluster, and 3) events with exactly one DT cluster. Events with two clusters are further categorized into categories with 2 CSC clusters, 2 DT clusters, and 1 CSC and 1 DT cluster.

The second category is based on the previous result using the endcap muon detectors in Ref. [32]

with a few changes, including explicitly excluding overlapping double cluster events and loosening the event-level selections to be consistent with other categories. The need to separate the endcap and barrel cluster is due to the different detector technologies used in the subdetectors, thus different information of the hits are available and different analysis strategies are used. The efficiency of the geometric acceptance and p_T^{miss} cut for each category are shown in Figure 4.

The following subsections describe the detailed event-selections for each category.

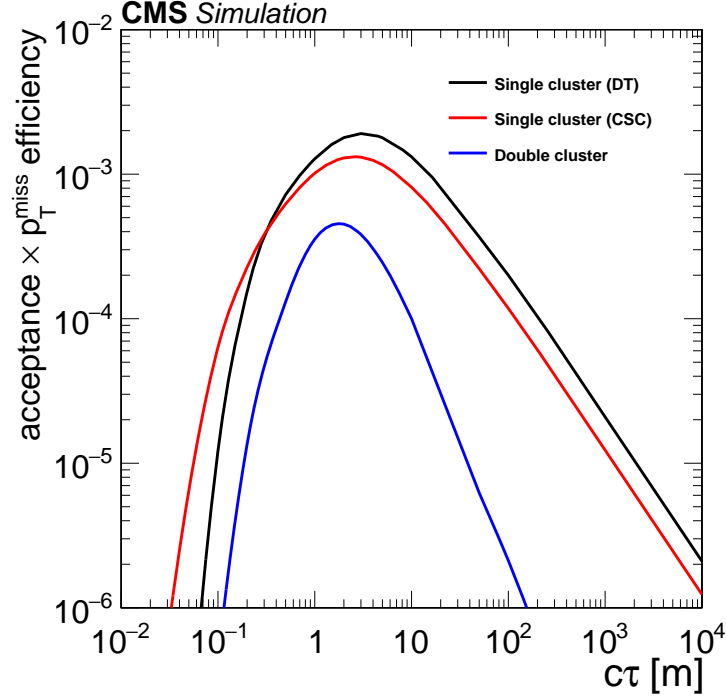


Figure 4: The efficiency of acceptance $\times p_T^{\text{miss}} \geq 200$ GeV cut are shown as a function of S lifetime, for a mass of 40 GeV.

5.1 Double clusters

In the double cluster category, we search for events where both LLPs decay in the muon detectors and produce muon detector showers. We split events into 3 categories depending on whether the cluster is in barrel or endcap: two DT clusters, two CSC clusters, or one CSC and one DT cluster. Requiring two muon system clusters significantly reduces the expected background, so the veto requirements in the double cluster category is much looser compared to the single cluster categories.

The main SM backgrounds include punch-through jets, muons that undergo bremsstrahlung, and decays of SM LLPs, such as the neutral kaon K_L^0 . To suppress background from punch-through jets or muon bremsstrahlung, we reject CSC clusters that have a jet or muon within a $\Delta R = \sqrt{(\Delta\eta)^2 + (\Delta\phi)^2} < 0.4$ cone and with jet $p_T > 30$ GeV or a global muon with matched tracks from the tracker and with $p_T > 30$ GeV. We reject DT clusters that have a jet or muon within a $\Delta R < 0.4$ cone and with jet $p_T > 50$ GeV or a muon passing loose identification criteria [59, 60] and with $p_T > 10$ GeV.

We veto CSC clusters that are entirely contained in the innermost rings of the ME1 station (ME1/1) and veto DT clusters that have more then 90% of the hits contained in the innermost

station (MB1), both of which have the least absorber material in front, larger number of background clusters in those stations.

We require the azimuthal angle between the cluster location and the \vec{p}_T^{miss} ($\Delta\phi_c$) to be less than 1 (1.2) for CSC(DT) clusters. For signal, $\Delta\phi_c$ peaks near zero because the large p_T^{miss} requirement tends to select highly boosted Higgs bosons for which the S and H momentum vectors are spatially close to each other. For the backgrounds, $\Delta\phi_c$ is uniformly distributed, since the cluster and \vec{p}_T^{miss} are independent.

Due to the differences in the sub-detectors, we further reject CSC clusters produced by out-of-time pileup by requiring the cluster time (t_{cluster}), defined as the average time of the hits in the cluster relative to the LHC clock, to be consistent with an in-time interaction ($-5.0 < t_{\text{cluster}} < 12.5$ ns). A larger time window is used at positive values to capture signal clusters with longer delays from slower moving LLPs. To reject clusters composed of hits from multiple bunch crossings, we require that the root mean square spread of a cluster's hit times is less than 20 ns.

For DT clusters, we reject clusters from muon bremsstrahlung by vetoing clusters that contain hits in all 4 stations and ratio of the number of hits in the minimum and maximum station is less than 0.4. Tracks from muons are likely to deposit similar number of hits in all 4 stations, while showers from LLP decays are likely to have hits more concentrated in 1 or 2 stations. To suppress background from cosmic ray muons, which produce hits in both upper and lower hemispheres of the muon barrel system, we reject DT clusters if there are at least 6 segments and at least 1 segment in every station found in the opposite hemisphere ($|\Delta\phi| > 2$) from the cluster.

To suppress background from cosmic ray muon showers, which produce hits in multiple regions of the CMS detector, we reject any event in which more than a quarter of DT and CSC ϕ -rings contain 50 or more hits.

Finally we select events that contain 2 clusters satisfying the above selection criteria for CSC and DT clusters. Depending on where the two clusters are, the events are categorized into: CSC-CSC, DT-DT, or DT-CSC categories. For signal events with two clusters, the ΔR between two LLPs, thus between the clusters, are usually small. For background the ΔR between clusters can be large, since the two clusters generally come from separate processes, especially for CSC-CSC and DT-CSC categories. Therefore, we require the ΔR between the two clusters to be less than 2 (2.5) for CSC-CSC (DT-CSC) category. Note that there is already an implicit $\Delta\phi$ cut between the two clusters by requiring both clusters to pass the $\Delta\phi_c$ selection. The ΔR cut is an additional selection that further requires two clusters to be close in η direction.

Finally the number of hits in the two clusters (N_{hits}) is used to make the final discrimination between signal and background. The distribution of N_{hits} remains high at large N_{hits} values for signal events, but for background events the distribution of N_{hits} decreases sharply with increasing N_{hits} values. We require $N_{\text{hits}} \geq 100$ (80) for CSC (DT) clusters.

For the backgrounds, N_{hits} for the two clusters are independent, enabling the use of a modified matrix (ABCD) method to predict the background yield in the signal-enriched region, as detailed in Section 6. For DT-CSC category, we use the matrix method, where the two variables are the N_{hits} of the DT and CSC cluster respectively. For CSC-CSC and DT-DT category, since the two variables are the same, we simply combine bin B and D, and perform a modified matrix method, consisting of only 3 bins. As illustrated in the cartoon in Figure 5, bin A, B, and C are events with 0, 1, and 2 clusters passing the N_{hits} cut, respectively.

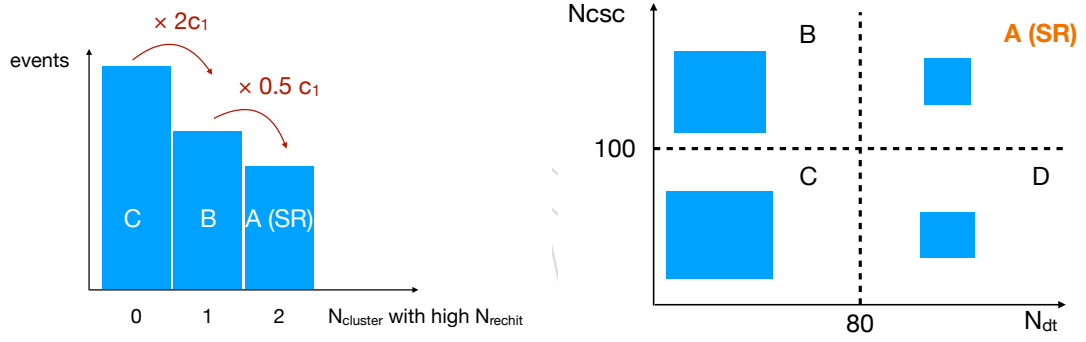


Figure 5: Cartoons illustrating the ABCD plane (left) for DT-CSC category and ABC plane (right) for DT-DT and CSC-CSC category. c_1 is the ratio for background cluster to pass and fail the N_{hits} cut. Bin A is the signal region for all categories.

5.2 Single CSC clusters

In the single CSC cluster category, we search for events where only one LLP is required to decay and produce displaced clusters in the endcap muon system. Due to the requirement of just one cluster, the background level is significantly higher, so we apply much tighter cluster veto requirements to achieve the same near-zero background level.

The cluster veto requirements are exactly the same as [32], only the event-level selections were changed to be inlined with the other two categories, and overlapping events with the double cluster category are removed and only counted in the double cluster category, which is the category with higher sensitivity.

As mentioned, the main SM backgrounds include punch-through jets, muons that undergo bremsstrahlung, and decays of SM LLPs, such as the neutral kaon K_L^0 . To suppress background from punch-through jets or muon bremsstrahlung, tighter cluster vetoes are applied compared to the double cluster category. We reject clusters that have a jet or muon within a $\Delta R < 0.4$ cone and with jet $p_T > 10$ GeV or muon $p_T > 20$ GeV. We veto clusters that have any hits in the two innermost rings of the ME1 station (ME1/1 and ME1/2), which have the least absorber material in front, or match any hit (with $\Delta R(\text{cluster}, \text{hit}) < 0.4$) in the RPCs located immediately next to ME1/2. In the region where the barrel and endcap muon detectors overlap ($0.8 < |\eta| < 1.2$), we veto any cluster matched to any track segment reconstructed in the innermost station of the DT detectors (MB1), or any hit in the RPCs situated in front of and behind MB1 matched to within $\Delta R(\text{cluster}, \text{segment}/\text{hit}) < 0.4$. Finally, we reject clusters with $|\eta| > 2.0$ to suppress the muon bremsstrahlung background that evaded the muon veto because of the high muon reconstruction and identification inefficiencies at larger $|\eta|$.

Same as the double cluster category, to suppress background from cosmic ray muon showers, which produce hits in multiple regions of the CMS detector, we reject any event in which more than a quarter of DT and CSC ϕ -rings contain 50 or more hits.

After the veto requirements are applied, the dominant background source consists of decays of SM LLPs, which are predominantly produced by pileup interactions and are independent of the primary interaction that yielded the large p_T^{miss} . These pileup interactions can occur concurrently with the primary interaction (in-time pileup) or in adjacent bunch crossings (out-of-time or OOT pileup), as shown in Figure 6. Clusters produced by OOT pileup are rejected by requiring the cluster time (t_{cluster}), defined as the average time of the hits in the cluster relative to the LHC clock, to be consistent with an in-time interaction ($-5.0 < t_{\text{cluster}} < 12.5$ ns). A larger time window is used at positive values to capture signal clusters with longer delays from slower moving LLPs. The time window requirement suppresses the background by a factor of 5. To reject clusters composed of hits from multiple bunch crossings, we require that the root mean square spread of a cluster's hit times is less than 20 ns.

There are several features that distinguish between signal and background clusters. Clusters from all background processes occur more often at larger values of $|\eta|$, as the effectiveness of the jet and muon vetoes decrease because of increasing reconstruction inefficiencies. Signal clusters often occupy more than one CSC station and occur more frequently in stations further away from the primary interaction point. A cluster identification algorithm was devised that makes successively more restrictive $|\eta|$ requirements as the number of CSC stations containing hits and the distance between the station and the primary interaction point decrease. The cluster identification algorithm has $\sim 80\%$ efficiency for clusters originating from S decays in the simulation, and suppresses the background by a factor of 3. The events that pass the cluster identification criteria are used to define the search region, and those that fail are used as an

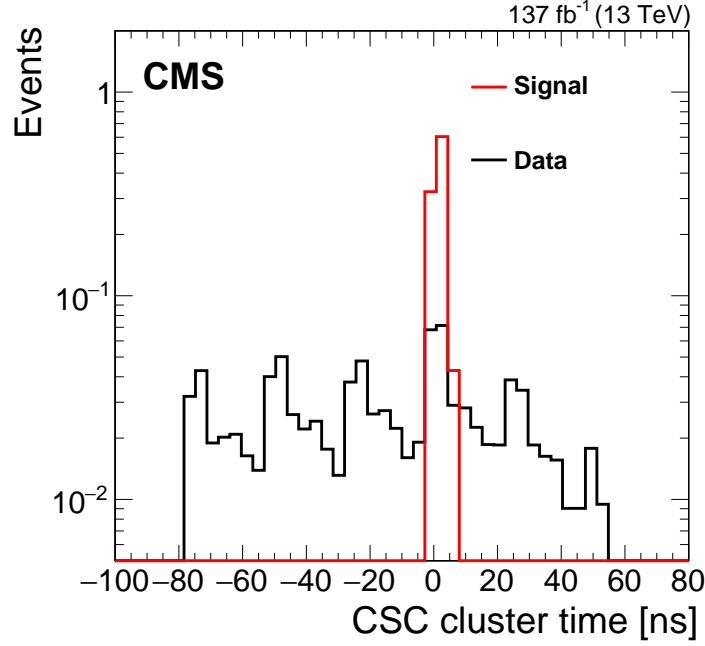


Figure 6: The signal and background shapes of cluster time are shown for S decaying to $d\bar{d}$ for a lifetime of 1 m and mass of 40 GeV.

additional in-time VR.

The number of hits in the cluster (N_{hits}) and the azimuthal angle between the cluster location and the \vec{p}_T^{miss} ($\Delta\phi_c$) are used to make the final discrimination between signal and background. The signal and background shape of the two discriminators are shown in Figure 7. The distribution of N_{hits} remains high at large N_{hits} values for signal events, but for background events the distribution of N_{hits} decreases sharply with increasing N_{hits} values. For signal, $\Delta\phi_c$ peaks near zero either because the \vec{p}_T^{miss} results from the same S decay that produced the cluster or the large p_T^{miss} requirement tends to select highly boosted Higgs bosons for which the S and H momentum vectors are spatially close to each other. For the backgrounds, $\Delta\phi_c$ is independent of N_{hits} , enabling the use of the matrix (ABCD) method to predict the background yield in the signal-enriched bin, as detailed in Section 6.

As illustrated in the cartoon in Figure 8: Bin A includes events with $\Delta\phi_c < 0.75$ and $N_{\text{hits}} > 130$; bin B includes events with $\Delta\phi_c \geq 0.75$ and $N_{\text{hits}} > 130$; bin C includes events with $\Delta\phi_c \geq 0.75$ and $N_{\text{hits}} \leq 130$; and bin D includes events with $\Delta\phi_c < 0.75$ and $N_{\text{hits}} \leq 130$.

5.3 Single DT clusters

In this section, we discuss the selections for the single DT cluster category. In the single DT cluster category, we search for events where only one LLP is required to decay and produce displaced clusters in the barrel muon system. Similar to the single CSC cluster category, the background level is significantly higher due to the requirement of just one cluster, so we apply much tighter cluster veto requirements to achieve the same near-zero background level.

For this category, overlapping events with the single CSC cluster category and double cluster category are removed and only counted in the double cluster category, to give precedence to category with higher sensitivity (double cluster) and minimize changes to previously published results (single CSC cluster).

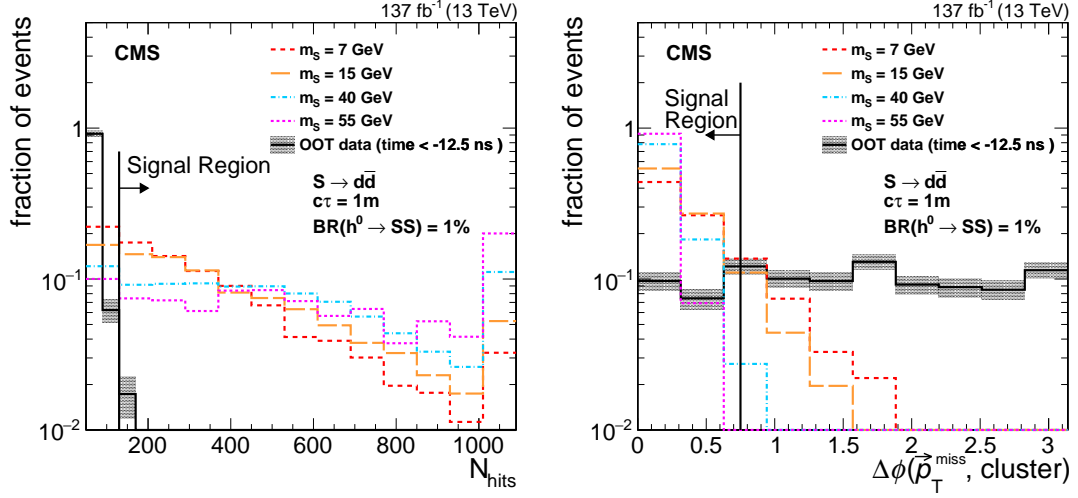


Figure 7: The shape of N_{hits} (left) and $\Delta\phi_c$ (right) are shown for S decaying to $d\bar{d}$ for a lifetime of 1 m and various masses.

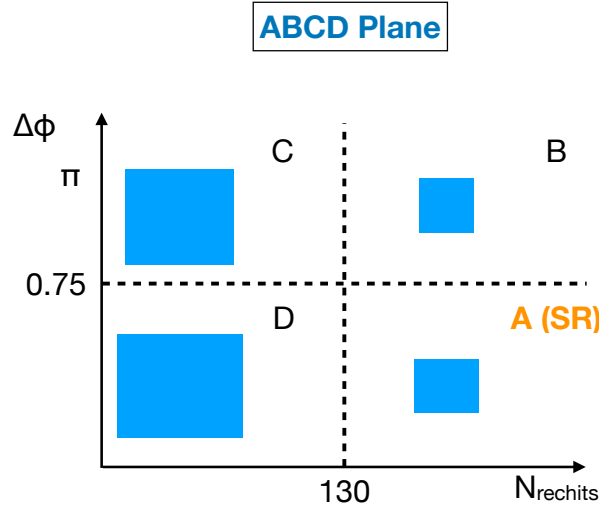


Figure 8: A cartoon illustrating the ABCD plane, where bin A is the signal region.

First, to remove high MET events due to mis-measured jets, we require the minimum of $|\Delta\phi(\text{jet}, \vec{p}_T^{\text{miss}})| > 0.6$, over all $p_T > 30$ GeV jets.

As mentioned, the main SM backgrounds include punch-through jets, muons that undergo bremsstrahlung, and decays of SM LLPs, such as the neutral kaon K_L^0 . To suppress background from punch-through jets or muon bremsstrahlung, tighter cluster vetoes are applied compared to the double cluster category. We reject clusters that have a jet or a muon within a $\Delta R < 0.4$ cone and with jet $p_T > 10$ GeV or muon passing loose identification criteria [59, 60] and with $p_T > 10$ GeV. In addition, we reject clusters that are within a $\Delta R < 1.2$ cone from the leading jet.

Furthermore, we reject clusters that have more than 1 hit from the innermost station, MB1, within $\Delta R < 0.4$ cone for all DT clusters and clusters that have more than 1 hit from the MB2 within $\Delta R < 0.4$ cone for DT clusters that have the maximum number of hits in MB3 and MB4.

To reject clusters from fake hits in the DTs, we require clusters to be matched to at least 1 RPC hit, from the same DT wheel and within $\Delta\phi < 0.5$.

To suppress background clusters from cosmic muons, we veto on clusters that have more than 8 hits in the MB1 stations in adjacent wheels within $\Delta\phi < \pi/4$ for all DT clusters and more than 8 hits in the MB2 stations in adjacent wheels within $\Delta\phi < \pi/4$ for DT clusters that have the maximum number of hits in MB3 and MB4. Furthermore, we look for DT segments that are far from the clusters with $\Delta R > 0.4$ in the upper or lower hemisphere of the DT wheels. We veto the cluster if more than 14 segments are found in either hemisphere or more than 10 segments are found in both hemispheres.

Similar to the single CSC cluster category, the number of hits in the cluster (N_{hits}) and the azimuthal angle between the cluster location and the \vec{p}_T^{miss} ($\Delta\phi_c$) are used to make the final discrimination between signal and background. We require $\Delta\phi_c < 1$ and $N_{\text{hits}} > 100$.

The signal and background shapes of the two discriminators are shown in Figure 9. The distribution of N_{hits} remains high at large N_{hits} values for signal events, but for background events the distribution of N_{hits} decreases sharply with increasing N_{hits} values. For signal, $\Delta\phi_c$ peaks near zero either because the \vec{p}_T^{miss} results from the same S decay that produced the cluster or the large p_T^{miss} requirement tends to select highly boosted Higgs bosons for which the S and H momentum vectors are spatially close to each other.

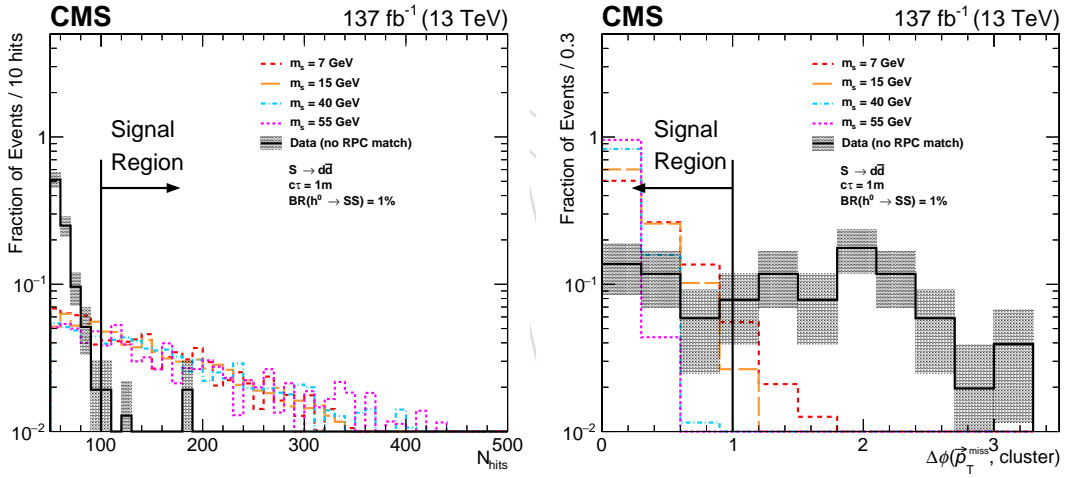


Figure 9: The shapes of N_{hits} (left) and $\Delta\phi_c$ (right) for DT clusters are shown for S decaying to $b\bar{b}$ for a lifetime of 10 m and various masses compared to the background distribution in a selection where the cluster is not matched to any RPC hits.

The remaining background components in the single DT cluster category consist of punch-through jets and pileup. For pile-up like backgrounds, $\Delta\phi_c$ is independent of N_{hits} , enabling the use of the matrix (ABCD) method to predict the background yield in the signal-enriched bin A. The number of punch-through jet background in bin A is predicted separately, as detailed in Section 6.

Finally, the DT clusters are categorized into 3 exclusive categories by the station that contains the most number of hits, including MB2, MB3, and MB4. These categories have different background compositions, where the punch-through jet background is more prominent in the stations that are closer to the interaction point.

6 Background estimation

As briefly mentioned in Section 5, the data-driven ABCD method is used for background estimation for all 3 categories. In addition, the single DT cluster category estimates the punch-through jet background separately. The following sub-sections detail the main background component, the background estimation method, and its validation for each category.

6.1 Double clusters

For background in the double clusters category, N_{hits} for the two clusters are independent, enabling the use of a modified matrix (ABCD) method to predict the background yield in the signal-enriched region.

For DT-CSC category, we use the matrix method, where the two variables are the N_{hits} of the DT and CSC cluster respectively. For CSC-CSC and DT-DT category, since the two variables are the same, we simply combine bin B and D, and perform a modified matrix method, consisting of only 3 bins. As illustrated in the cartoon in Figure 5, bin A, B, and C are events with 0, 1, and 2 clusters passing the N_{hits} cut, respectively.

To validate the background estimation method, we defined two validation regions: the inverted N_{hits} region and the inverted $\Delta\phi_c$ region. The inverted N_{hits} validation region is defined by inverting the N_{hits} requirements for both clusters passing all other cluster-level selections. The inverted $\Delta\phi_c$ validation region is defined by inverting the $\Delta\phi_c$ requirement of both clusters passing all other cluster-level selections. To probe signal-like events in the inverted $\Delta\phi_c$ validation region, we additionally require that $\Delta\phi(\text{cluster1}, \text{cluster2})$ to be < 2 and < 2.4 for DT-DT and CSC-CSC category, respectively. This validation region allows us to test for any non-negligible high N_{hits} tails that cannot be accessed in the inverted N_{hits} validation region.

The background estimation agrees with the number of observed background events in both validation regions and all 3 categories, as shown in Table 1.

Table 1: Validation of the ABCD method in both validation regions. The uncertainty of the prediction is the statistical uncertainty propagated from bin A, B, and C.

Category	Validation region	A(SR)	B	C		Prediction
DT-DT	inverted N_{hits}	0	1	11		0.02 ± 0.05
	inverted $\Delta\phi$	0	1	2		0.12 ± 0.27
CSC-CSC	inverted N_{hits}	0	2	8		0.12 ± 0.18
	inverted $\Delta\phi$	0	2	4		0.25 ± 0.38
Category	Validation region	A(SR)	B	C	D	Prediction
DT-CSC	inverted N_{hits}	0	0	34	6	0 ± 0
	inverted $\Delta\phi$	0	3	16	1	0.19 ± 0.22

6.2 Single CSC clusters

For single CSC category, we use the matrix method, where the two variables are $\Delta\phi_c$ and N_{hits} . The background estimation procedure is validated using events in two separate validation regions: one in the out-of-time region, where $t_{\text{cluster}} < -12.5$ ns, and one in the in-time region, where the clusters failing the cluster identification are selected, as shown in Table 2.

Table 2: Validation of the ABCD method in both validation regions. The uncertainty of the prediction is the statistical uncertainty propagated from bin B, C, and D.

Validation region	A(SR)	B	C	D	Prediction ($\frac{B \times D}{C}$)
Out-of-time region	3	8	445	121	2.18 ± 0.8
In-time region	2	7	328	88	1.88 ± 0.74

6.3 Single DT clusters

The background in the single DT cluster category is composed of punch-through jet and low p_T particles from pileup. To estimate the background from the low p_T particles, the ABCD method is used. The background prediction is validated in a pileup-enriched validation region, where the loose identification criteria on the leading jet is inverted, filters that reject non-collision background, RPC matching, and $\Delta\phi_c$ requirement are removed, as shown in Table 3.

To estimate the punch-through jet background that is not predicted by the ABCD method in the signal region, we multiply the expected punch-through jet background in the MB1/MB2 hit veto inverted region, measured by the non-closure of the ABCD method in the MB1/MB2 hit veto inverted region, by the MB1/MB2 hit veto efficiency to extrapolate the number of punch-through jet background in the signal region. For clusters in MB2, only MB1 veto is applied, so only MB1 veto is inverted for the punch-through jet background measurement and MB1 efficiency is measured. For clusters in MB3 and MB4, both MB1 and MB2 vetoes are inverted for the punch-through jet background measurement and the MB1 and MB2 hit veto efficiencies are measured.

The number of punch-through jet background events is measured by the non-closure of the ABCD method in the inverted MB1/MB2 veto region, with enriched punch-through jet background. We measured 22 ± 7 , 7 ± 3 , and 2.0 ± 1.7 punch-through jet background for MB2, MB3, and MB4 cluster, respectively.

The MB1/MB2 hit veto efficiency is measured in another punch-through jet enriched region, by selecting clusters that have a jet with $p_T > 10$ GeV within a $\Delta R < 0.4$ cone, as a function of the matched jet p_T . The MB1/MB2 hit veto efficiency is measured separately for clusters in each station, as shown in Figure 10. The MB1 hit veto efficiency in the signal region is extrapolated by fitting the measured efficiency with the sum of an exponential and constant function for MB2 clusters and a constant function for MB3 and MB4 clusters.

The extrapolated MB1/MB2 veto efficiency is 0.23 ± 0.02 , 0.38 ± 0.07 , and 0.3 ± 0.1 for MB2, MB3, and MB4 cluster, respectively. Using the extrapolated MB1/MB2 veto efficiency and the punch-through jet background measured in MB1/MB2 veto inverted region, results in a predicted punch-through jet background of 6.5 ± 2.1 , 4.4 ± 2.2 , and 0.8 ± 0.9 for MB2, MB3, and MB4 cluster, respectively, in addition to the ABCD background prediction.

The punch-through jet background prediction method is validated by predicting background clusters that are matched to 2-5 MB1 or 2-5 MB1 hits, instead of < 2 MB1 or < 2 MB2 hits in the signal region.

Table 3: Event yields in ABCD regions for two background-enriched selection. Bins C and D for MB3 and MB4 categories are combined to improve the statistics in the two regions. The final ABCD fit in the signal region will also be performed with those bins combined.

Cluster station	A(SR)	B	C	D	Prediction ($\frac{B \times D}{C}$)
MB2	3	2	130	82	1.3 ± 0.9
MB3	1	1	20	11	0.4 ± 0.4
MB4	1	0			0.0 ± 1.1

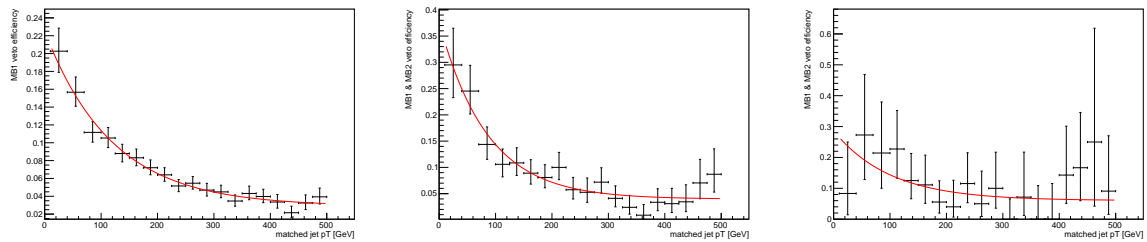


Figure 10: The MB1/MB2 veto efficiency as a function of matched jet p_T for clusters in MB2 (left), MB3 (center), and MB4 (right).

7 Signal Modeling

The simulation modelling of the cluster reconstruction efficiency, cluster-level selections, and the veto efficiencies are detailed in this section. The accuracy of the simulation prediction for the clusters relies on its ability to model correctly the response of the muon detectors in an environment with multiple particles, each producing a large number of secondary shower particles. This aspect is validated by measuring clusters produced in $Z \rightarrow \mu^+ \mu^-$ data events, where one of the muons undergoes bremsstrahlung in the muon detectors and the associated photon produces an electromagnetic shower, and the associated systematic uncertainty is taken into account in the overall uncertainty on the reconstruction and selection efficiencies.

On the other hand, the simulation modelling of the veto efficiencies, including the jet, muon, ME1, MB1, and RPC hit vetoes, are predominantly determined by the simulation of the jets and muons, presence of pileup particles and random noise. The veto efficiencies are measured by randomly sampling the (η, ϕ) locations of clusters from the signal distribution and evaluating whether a jet/muon or ME1/MB1/RPC hit has been observed within a $\Delta R < 0.4$ cone about the cluster's location, using $Z \rightarrow \mu^+ \mu^-$ data events with the two muons from the Z decay removed.

7.1 CSC cluster selection

For CSC clusters in the single CSC cluster category, the systematic uncertainty are dominated by the cluster reconstruction efficiency and the cluster identification efficiency, which amounts to a total of 8% systematic uncertainty.

The loss of veto efficiency is dominated by the muon veto, which is affected by muon segments produced by particles resulting from the LLP decay itself. This contribution is further validated using a control sample of clusters matched to trackless jets made to resemble the signal LLP decay by requiring the neutral energy fraction to be larger than 95%. A 10% correction is applied to the signal efficiency to account for the simulation's mismodeling of the vetoes.

For CSC clusters in the double cluster category, looser selections are applied, so the systematic uncertainty are dominated by the cluster time spread cut, which amounts to 10% for the CSC-CSC category and 5% for the DT-CSC category. Furthermore, in the double cluster category, the jet and muon vetoes are implemented with tighter identification criteria, so the presence of jets and muons are well-modelled and no corrections and uncertainty are assigned.

7.2 DT cluster selection

For the DT clusters in the single DT cluster category, the systematic uncertainty is dominated by the cluster reconstruction efficiency and the RPC hit matching efficiency. The cluster reconstruction efficiency uncertainty is measured to be 15%. A 10% correction and 5% uncertainty are applied to the signal efficiency to account for the mismodelling of the RPC hits.

Furthermore, the MB1 veto efficiency is also measured by randomly sampling the locations of the clusters from the signal distribution and evaluating whether a MB1 hit has been matched. A 10% correction and 7% uncertainty are applied to the signal efficiency to account for the mismodelling of the MB1 hits.

For the DT clusters in the double cluster category, the signal systematic uncertainty is dominated by the cluster reconstruction efficiency, which is measured to be 3% and 1%.

8 Systematic uncertainties

The dominant source of signal uncertainty is missing higher order QCD corrections, which amounts to 21% for the gluon fusion production. The other main sources of uncertainties include the signal modelling of the cluster reconstruction and selections, as detailed in Section 7, jet energy scale (3–6%) [61], PDFs (3%), pileup modelling (2%), integrated luminosity (1.6%) [62–64], and simulation sample statistical uncertainties (3–5%).

Since the background prediction is data driven and the estimation methods are validated, as detailed in Section 6, no background systematic uncertainties are assigned.

9 Results and interpretation

In this section, we show the result of each category and the interpretation of the combined results of 3 categories in the Twin Higgs and hidden valley models.

9.1 Double cluster category

The result of the double cluster category is shown in Table 4. We observed no statistically significant deviation with respect to the SM prediction. The signal and data distributions of N_{clusters} passing the N_{hits} cuts are shown in Fig. 11.

Table 4: Number of background events predicted and observed by the ABCD method.

category	fit	A(SR)	B	C	
DT-DT	Background-only fit	0.04	1	6	
	Observation	/	1	6	
CSC-CSC	Background-only fit	0.08	1	3	
	Observation	/	1	3	
category	fit	A(SR)	B	C	D
DT-CSC	Background-only fit	0.14	2	14	1
	Observation	/	2	14	1

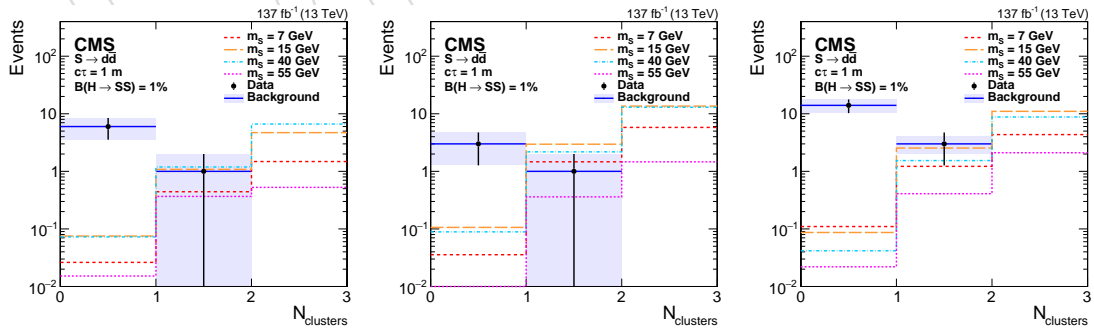


Figure 11: The signal (assuming $\mathcal{B}(h^0 \rightarrow SS) = 1\%$, $S \rightarrow d\bar{d}$, and $c\tau = 1$ m) and data distributions of N_{clusters} passing the N_{hits} cuts in the search region for CSC-CSC (left), DT-DT (center), and DT-CSC (right) categories. For CSC-CSC and DT-DT, events with 0 clusters include events in bin C, events with 1 cluster include events in bin B, and events with 2 clusters include events in bin A. For DT-CSC category, events with 0 clusters include events in bin C, events with 1 cluster include events in bin B and D, and events with 2 clusters include events in bin A.

9.2 Single CSC cluster category

The result of the single CSC cluster category is shown in Table 5. We observed no statistically significant deviation with respect to the SM prediction.

Table 5: Number of background events predicted and observed by the ABCD method.

	A(SR)	B	C	D
Background-only fit	1.8 ± 0.9	4.2 ± 1.9	117 ± 11	50 ± 7
Observed	3	3	118	49

The signal and data distributions of N_{hits} ($\Delta\phi_c$) in the bins A and D (A and B) are shown in Fig. 12.

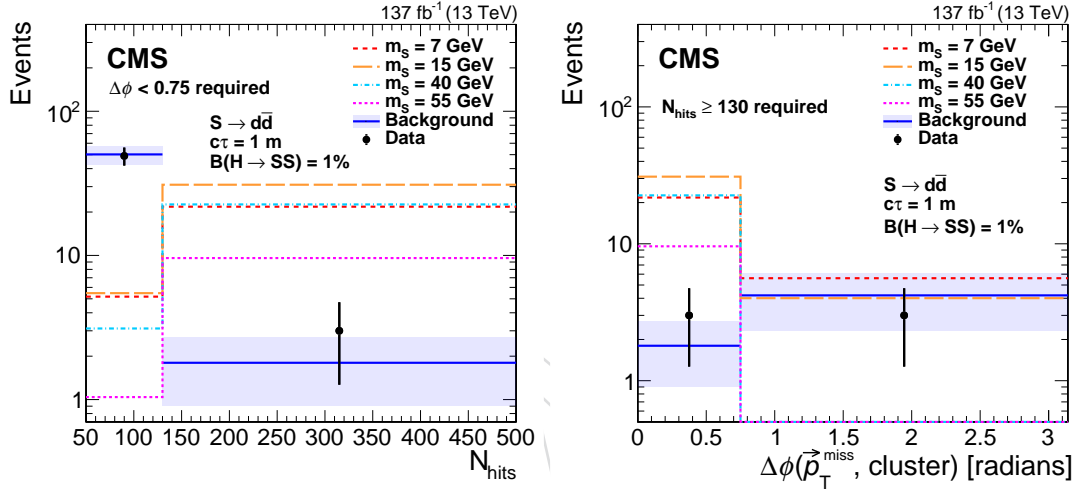


Figure 12: Distributions of N_{hits} (left) and $\Delta\phi_c$ (right) in the search region. The background predicted by the fit is shown in blue with the shaded region showing the fitted uncertainty. The expected signal with $\mathcal{B}(h^0 \rightarrow SS) = 1\%$, $S \rightarrow d\bar{d}$, and $c\tau = 1$ m is shown for m_S of 7, 15, 40, and 55 GeV in various colors and dotted lines. The N_{hits} distribution includes only events in bins A and D, while the $\Delta\phi_c$ includes only events in bins A and B. The last bin in the N_{hits} distributions includes overflow events.

9.3 Single DT cluster category

The result of the single DT cluster category is shown in Table 6. We observed no statistically significant deviation with respect to the SM prediction.

Table 6: Number of background events predicted and observed by the ABCD method.

category	fit	A (punch-through)	A(uncorrelated)	B	C	D
Background-only fit	MB2	6.5 ± 2.1	3.2	5	119	77
	MB3	4.4 ± 2.2	1.3	1	6	8
	MB4	0.8 ± 0.9	0.0	0		
Observation	MB2	/	/	5	119	71
	MB3	/	/	1	6	
	MB4	/	/	0		8

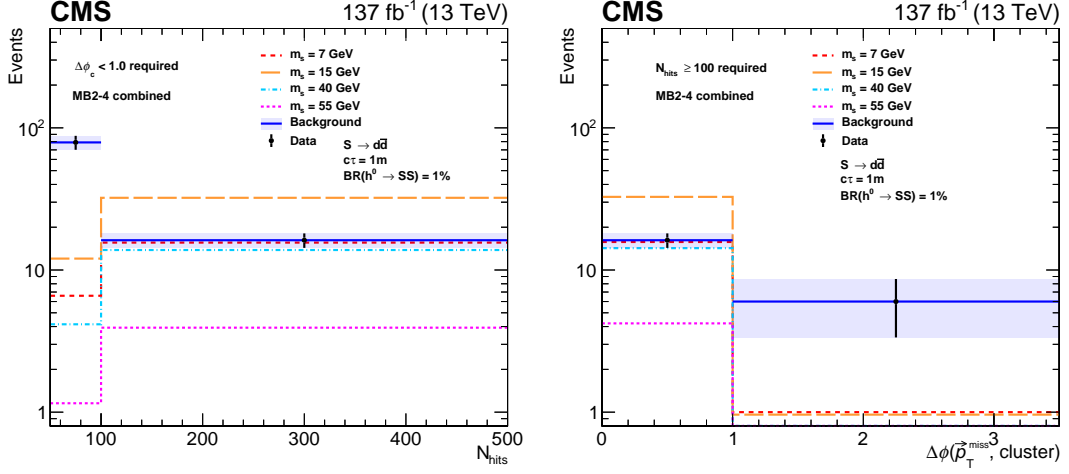


Figure 13: Distributions of N_{hits} (left) and $\Delta\phi_c$ (right) in the search region. The background predicted by the fit is shown in blue with the shaded region showing the fitted uncertainty. The expected signal with $\mathcal{B}(h^0 \rightarrow SS) = 1\%$, $S \rightarrow d\bar{d}$, and $c\tau = 1$ m is shown for m_S of 7, 15, 40, and 55 GeV in various colors and dotted lines. The N_{hits} distribution includes only events in bins A and D, while the $\Delta\phi_c$ includes only events in bins A and B. The last bin in the N_{hits} distributions includes overflow events. **data currently set to background prediction, will be updated once unblinded.**

9.4 Interpretations

In this section, we show the interpretations of the Twin Higgs model and the hidden valley models.

We evaluate 95% confidence level (CL) limits on the branching fraction $\mathcal{B}(h^0 \rightarrow SS)$ and $\mathcal{B}(h^0 \rightarrow \Psi\Psi)$ for both the Twin Higgs and hidden valley models using the modified frequentist criterion CL_s [65–67] with the profile likelihood ratio test statistic.

The upper limits for the Twin Higgs model are shown in Fig. 14 for the $S \rightarrow d\bar{d}$, $S \rightarrow \pi^0\pi^0$, and $S \rightarrow \tau^+\tau^-$ decay modes, as a function of $c\tau$ for a selection of values of m_S .

The simulated signal samples that were generated were limited to LLP mass above 0.4 GeV. Therefore, to extrapolate the analysis sensitivity to lower masses, we validated the the signal efficiency is the same for LLPs that have the same product of LLP masses and proper lifetimes for 0.4 GeV to 4 GeV LLP masses and both fully hadronic ($S \rightarrow \pi^+\pi^-$) and fully leptonic ($S \rightarrow e^+e^-$) decays for all 3 categories.

We show the upper limits, extending as low as 10 MeV, as a function of both mass and $c\tau$ for the $S \rightarrow d\bar{d}$, $S \rightarrow \pi^0\pi^0$, and $S \rightarrow \tau^+\tau^-$ decay modes in Fig. 15. Finally, we show the upper limits as a function of both mass and $c\tau$, assuming the S decay mode in Ref. [68] in Fig. 16.

The upper limits for the hidden valley models are shown in Fig. 17 for the gluon, photon, and vector portal, as a function of $c\tau$ for a selection of values of m_Ψ . $(x_{i\omega}, x_{i\Lambda}) = (2.5, 2.5), (2.5, 1), (1, 1)$.

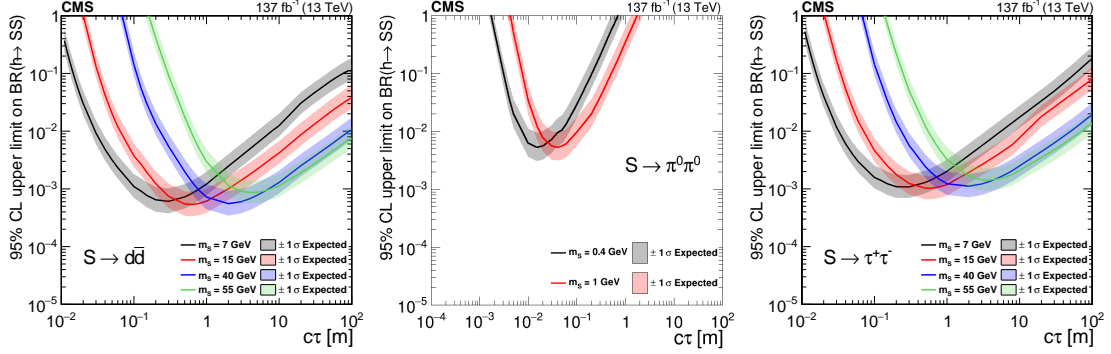


Figure 14: The 95% CL expected (dotted curves) and observed (solid curves) upper limits on the branching fraction $\mathcal{B}(h^0 \rightarrow SS)$ as functions of $c\tau$ for the $S \rightarrow d\bar{d}$ (left), $S \rightarrow \pi^0\pi^0$ (center), and $S \rightarrow \tau^+\tau^-$ (right) decay modes. The exclusion limits are shown for different mass hypotheses: 0.4, 1, 3, 7, 15, 40, and 55 GeV.

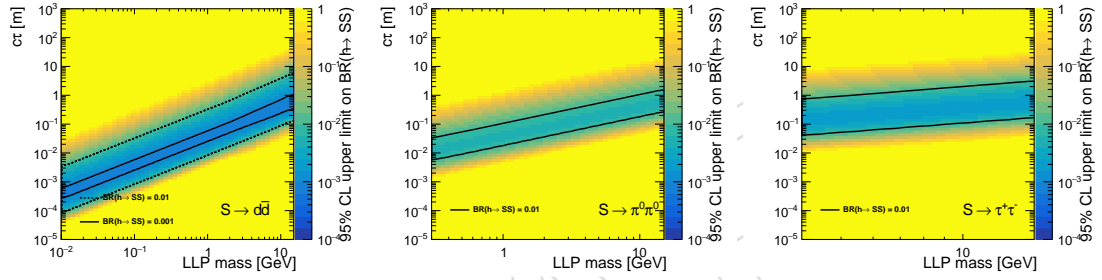


Figure 15: The 95% CL observed upper limits on the branching fraction $\mathcal{B}(h^0 \rightarrow SS)$ as functions of mass and $c\tau$ for the $S \rightarrow d\bar{d}$ (left), $S \rightarrow \pi^0\pi^0$ (center), and $S \rightarrow \tau^+\tau^-$ (right) decay modes.

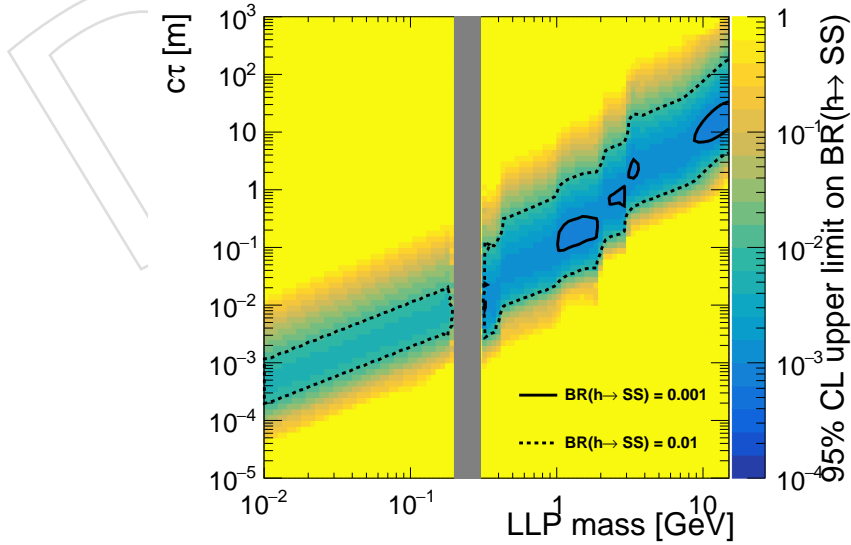


Figure 16: The 95% CL observed upper limits on the branching fraction $\mathcal{B}(h^0 \rightarrow SS)$ as functions of mass and $c\tau$. We do not set limit for S mass between 0.2 and 0.3 GeV (gray region), where S decays to di-muons.

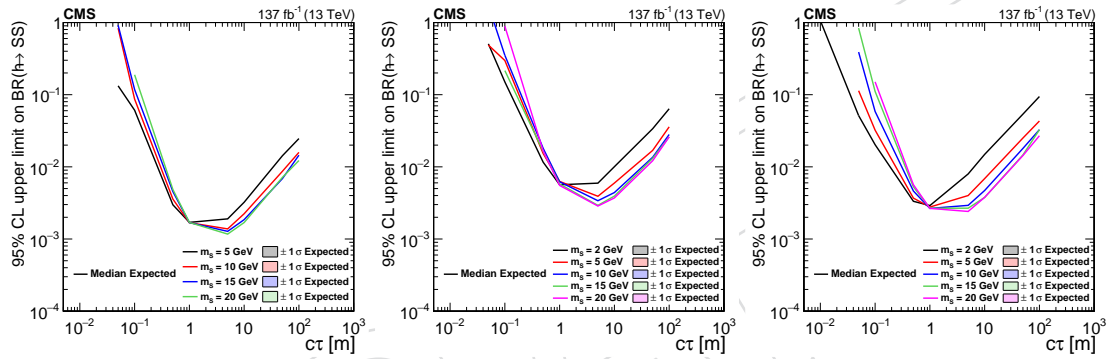


Figure 17: The 95% CL expected (dotted curves) and observed (solid curves) upper limits on the branching fraction $\mathcal{B}(h^0 \rightarrow \Psi\Psi)$ as functions of $c\tau$ for the gluon portal (left) assuming $(x_{i\omega}, x_{i\Lambda}) = (2.5, 1)$, photon portal (center) assuming $(x_{i\omega}, x_{i\Lambda}) = (2.5, 1)$, and vector portal (right) assuming $(x_{i\omega}, x_{i\Lambda}) = (1, 1)$. The exclusion limits are shown for different mass hypotheses: 2, 5, 10, 15, and 20 GeV.

10 Summary

In summary, proton-proton collision data at $\sqrt{s} = 13$ TeV recorded by the CMS experiment in 2016–2018, corresponding to an integrated luminosity of 137 fb^{-1} , have been used to conduct the first search for beyond the standard model (SM) long-lived particles (LLPs) using both the barrel and endcap CMS muon detectors as calorimeters. Based on a unique detector signature, the search is largely model-independent, with sensitivity to a broad range of LLP decay modes and to LLP masses below GeV. With the excellent shielding provided by the inner CMS detector, the background is suppressed to a low level and a search for both single and double LLP decays are possible.

No significant deviation from the SM background is observed, and the most stringent limits on the branching fraction of Higgs boson to LLP are set for proper decay lengths. This search also sets the first LHC limits on dark QCD that couples to the Higgs, sensitive to branching fraction of Higgs boson to dark quarks as low as 10^{-3} .

Acknowledgments

References

- [1] G. F. Giudice and A. Romanino, “Split supersymmetry”, *Nucl. Phys. B* **699** (2004) 65, doi:10.1016/j.nuclphysb.2004.08.001, arXiv:hep-ph/0406088. [Erratum: doi:10.1016/j.nuclphysb.2004.11.048].
- [2] J. L. Hewett, B. Lillie, M. Masip, and T. G. Rizzo, “Signatures of long-lived gluinos in split supersymmetry”, *JHEP* **09** (2004) 070, doi:10.1088/1126-6708/2004/09/070, arXiv:hep-ph/0408248.
- [3] N. Arkani-Hamed, S. Dimopoulos, G. F. Giudice, and A. Romanino, “Aspects of split supersymmetry”, *Nucl. Phys. B* **709** (2005) 3, doi:10.1016/j.nuclphysb.2004.12.026, arXiv:hep-ph/0409232.
- [4] P. Gambino, G. F. Giudice, and P. Slavich, “Gluino decays in split supersymmetry”, *Nucl. Phys. B* **726** (2005) 35, doi:10.1016/j.nuclphysb.2005.08.011, arXiv:hep-ph/0506214.
- [5] A. Arvanitaki, N. Craig, S. Dimopoulos, and G. Villadoro, “Mini-split”, *JHEP* **02** (2013) 126, doi:10.1007/JHEP02(2013)126, arXiv:1210.0555.
- [6] N. Arkani-Hamed et al., “Simply unnatural supersymmetry”, 2012. arXiv:1212.6971.
- [7] P. Fayet, “Supergauge invariant extension of the Higgs mechanism and a model for the electron and its neutrino”, *Nucl. Phys. B* **90** (1975) 104, doi:10.1016/0550-3213(75)90636-7.
- [8] G. R. Farrar and P. Fayet, “Phenomenology of the production, decay, and detection of new hadronic states associated with supersymmetry”, *Phys. Lett. B* **76** (1978) 575, doi:10.1016/0370-2693(78)90858-4.
- [9] S. Weinberg, “Supersymmetry at ordinary energies. Masses and conservation laws”, *Phys. Rev. D* **26** (1982) 287, doi:10.1103/PhysRevD.26.287.
- [10] R. Barbier et al., “R-parity violating supersymmetry”, *Phys. Rept.* **420** (2005) 1, doi:10.1016/j.physrep.2005.08.006, arXiv:hep-ph/0406039.

- [11] G. F. Giudice and R. Rattazzi, “Theories with gauge mediated supersymmetry breaking”, *Phys. Rept.* **322** (1999) 419, doi:10.1016/S0370-1573(99)00042-3, arXiv:hep-ph/9801271.
- [12] P. Meade, N. Seiberg, and D. Shih, “General gauge mediation”, *Prog. Theor. Phys. Suppl.* **177** (2009) 143, doi:10.1143/PTPS.177.143, arXiv:0801.3278.
- [13] M. Buican, P. Meade, N. Seiberg, and D. Shih, “Exploring general gauge mediation”, *JHEP* **03** (2009) 016, doi:10.1088/1126-6708/2009/03/016, arXiv:0812.3668.
- [14] J. Fan, M. Reece, and J. T. Ruderman, “Stealth supersymmetry”, *JHEP* **11** (2011) 012, doi:10.1007/JHEP11(2011)012, arXiv:1105.5135.
- [15] J. Fan, M. Reece, and J. T. Ruderman, “A stealth supersymmetry sampler”, *JHEP* **07** (2012) 196, doi:10.1007/JHEP07(2012)196, arXiv:1201.4875.
- [16] M. J. Strassler and K. M. Zurek, “Echoes of a hidden valley at hadron colliders”, *Phys. Lett. B* **651** (2007) 374, doi:10.1016/j.physletb.2007.06.055, arXiv:hep-ph/0604261.
- [17] M. J. Strassler and K. M. Zurek, “Discovering the Higgs through highly-displaced vertices”, *Phys. Lett. B* **661** (2008) 263, doi:10.1016/j.physletb.2008.02.008, arXiv:hep-ph/0605193.
- [18] T. Han, Z. Si, K. M. Zurek, and M. J. Strassler, “Phenomenology of hidden valleys at hadron colliders”, *JHEP* **07** (2008) 008, doi:10.1088/1126-6708/2008/07/008, arXiv:0712.2041.
- [19] Y. Cui, L. Randall, and B. Shuve, “A WIMPy baryogenesis miracle”, *JHEP* **04** (2012) 075, doi:10.1007/JHEP04(2012)075, arXiv:1112.2704.
- [20] Y. Cui and R. Sundrum, “Baryogenesis for weakly interacting massive particles”, *Phys. Rev. D* **87** (2013) 116013, doi:10.1103/PhysRevD.87.116013, arXiv:1212.2973.
- [21] Y. Cui and B. Shuve, “Probing baryogenesis with displaced vertices at the LHC”, *JHEP* **02** (2015) 049, doi:10.1007/JHEP02(2015)049, arXiv:1409.6729.
- [22] D. Smith and N. Weiner, “Inelastic dark matter”, *Phys. Rev. D* **64** (2001) 043502, doi:10.1103/PhysRevD.64.043502, arXiv:hep-ph/0101138.
- [23] Z. Chacko, H.-S. Goh, and R. Harnik, “Natural electroweak breaking from a mirror symmetry”, *Phys. Rev. Lett.* **96** (2006) 231802, doi:10.1103/PhysRevLett.96.231802, arXiv:hep-ph/0506256.
- [24] D. Curtin and C. B. Verhaaren, “Discovering uncolored naturalness in exotic Higgs decays”, *JHEP* **12** (2015) 072, doi:10.1007/JHEP12(2015)072, arXiv:1506.06141.
- [25] H.-C. Cheng, S. Jung, E. Salvioni, and Y. Tsai, “Exotic quarks in twin Higgs models”, *JHEP* **03** (2016) 074, doi:10.1007/JHEP03(2016)074, arXiv:1512.02647.
- [26] N. Craig, A. Katz, M. Strassler, and R. Sundrum, “Naturalness in the dark at the LHC”, *JHEP* **07** (2015) 105, doi:10.1007/JHEP07(2015)105, arXiv:1501.05310.
- [27] M. J. Strassler, “On the phenomenology of hidden valleys with heavy flavor”, 2008. arXiv:0806.2385.

- [28] J. E. Juknevich, D. Melnikov, and M. J. Strassler, “A pure-glue hidden valley I. states and decays”, *JHEP* **07** (2009) 055, doi:10.1088/1126-6708/2009/07/055, arXiv:0903.0883.
- [29] CMS Collaboration, “Search for long-lived particles using displaced jets in proton-proton collisions at $\sqrt{s} = 13$ TeV”, 2020. arXiv:2012.01581. Submitted to *Phys. Rev. D*.
- [30] ATLAS Collaboration, “Search for long-lived particles produced in pp collisions at $\sqrt{s} = 13$ TeV that decay into displaced hadronic jets in the ATLAS muon spectrometer”, *Phys. Rev. D* **99** (2019) 052005, doi:10.1103/PhysRevD.99.052005, arXiv:1811.07370.
- [31] ATLAS Collaboration, “Search for events with a pair of displaced vertices from long-lived neutral particles decaying into hadronic jets in the ATLAS muon spectrometer in pp collisions at $\sqrt{s}=13$ TeV”, *Phys. Rev. D* **106** (2022), no. 3, 032005, doi:10.1103/PhysRevD.106.032005, arXiv:2203.00587.
- [32] CMS Collaboration, “Search for Long-Lived Particles Decaying in the CMS End Cap Muon Detectors in Proton-Proton Collisions at $\sqrt{s}=13$ TeV”, *Phys. Rev. Lett.* **127** (2021), no. 26, 261804, doi:10.1103/PhysRevLett.127.261804, arXiv:2107.04838.
- [33] S. Knapen, J. Shelton, and D. Xu, “Perturbative benchmark models for a dark shower search program”, *Phys. Rev. D* **103** (2021), no. 11, 115013, doi:10.1103/PhysRevD.103.115013, arXiv:2103.01238.
- [34] “HEPData record for this analysis”, 2021. doi:10.17182/hepdata.104408.
- [35] CMS Collaboration, “The CMS experiment at the CERN LHC”, *JINST* **3** (2008) S08004, doi:10.1088/1748-0221/3/08/S08004.
- [36] CMS Collaboration, “Performance of the CMS cathode strip chambers with cosmic rays”, *JINST* **5** (2010) T03018, doi:10.1088/1748-0221/5/03/T03018, arXiv:0911.4992.
- [37] CMS Collaboration, “Performance of the CMS Level-1 trigger in proton-proton collisions at $\sqrt{s} = 13$ TeV”, *JINST* **15** (2020) P10017, doi:10.1088/1748-0221/15/10/P10017, arXiv:2006.10165.
- [38] CMS Collaboration, “The CMS trigger system”, *JINST* **12** (2017) P01020, doi:10.1088/1748-0221/12/01/P01020, arXiv:1609.02366.
- [39] P. Nason, “A new method for combining NLO QCD with shower Monte Carlo algorithms”, *JHEP* **11** (2004) 040, doi:10.1088/1126-6708/2004/11/040, arXiv:hep-ph/0409146.
- [40] S. Frixione, P. Nason, and C. Oleari, “Matching NLO QCD computations with parton shower simulations: the POWHEG method”, *JHEP* **11** (2007) 070, doi:10.1088/1126-6708/2007/11/070, arXiv:0709.2092.
- [41] S. Alioli, P. Nason, C. Oleari, and E. Re, “A general framework for implementing NLO calculations in shower Monte Carlo programs: the POWHEG BOX”, *JHEP* **06** (2010) 043, doi:10.1007/JHEP06(2010)043, arXiv:1002.2581.

- [42] E. Re, “Single-top Wt-channel production matched with parton showers using the POWHEG method”, *Eur. Phys. J. C* **71** (2011) 1547, doi:10.1140/epjc/s10052-011-1547-z, arXiv:1009.2450.
- [43] L. Carloni, J. Rathsmann, and T. Sjostrand, “Discerning Secluded Sector gauge structures”, *JHEP* **04** (2011) 091, doi:10.1007/JHEP04(2011)091, arXiv:1102.3795.
- [44] L. Carloni and T. Sjostrand, “Visible Effects of Invisible Hidden Valley Radiation”, *JHEP* **09** (2010) 105, doi:10.1007/JHEP09(2010)105, arXiv:1006.2911.
- [45] T. Sjöstrand et al., “An introduction to PYTHIA 8.2”, *Comput. Phys. Commun.* **191** (2015) 159, doi:10.1016/j.cpc.2015.01.024, arXiv:1410.3012.
- [46] CMS Collaboration, “Event generator tunes obtained from underlying event and multiparton scattering measurements”, *Eur. Phys. J. C* **76** (2016) 155, doi:10.1140/epjc/s10052-016-3988-x, arXiv:1512.00815.
- [47] CMS Collaboration, “Extraction and validation of a new set of CMS PYTHIA8 tunes from underlying-event measurements”, *Eur. Phys. J. C* **80** (2020) 4, doi:10.1140/epjc/s10052-019-7499-4, arXiv:1903.12179.
- [48] NNPDF Collaboration, “Parton distributions for the LHC Run II”, *JHEP* **04** (2015) 040, doi:10.1007/JHEP04(2015)040, arXiv:1410.8849.
- [49] NNPDF Collaboration, “Parton distributions from high-precision collider data”, *Eur. Phys. J. C* **77** (2017) 663, doi:10.1140/epjc/s10052-017-5199-5, arXiv:1706.00428.
- [50] GEANT4 Collaboration, “GEANT4—a simulation toolkit”, *Nucl. Instrum. Meth. A* **506** (2003) 250, doi:10.1016/S0168-9002(03)01368-8.
- [51] M. Ester, H.-P. Kriegel, J. Sander, and X. Xu, “A density-based algorithm for discovering clusters in large spatial databases with noise”, in *Proceedings of the Second International Conference on Knowledge Discovery and Data Mining*, p. 226. Association for the Advancement of Artificial Intelligence, 1996.
- [52] CMS Collaboration, “Particle-flow reconstruction and global event description with the CMS detector”, *JINST* **12** (2017) P10003, doi:10.1088/1748-0221/12/10/P10003, arXiv:1706.04965.
- [53] M. Cacciari, G. P. Salam, and G. Soyez, “The anti- k_T jet clustering algorithm”, *JHEP* **04** (2008) 063, doi:10.1088/1126-6708/2008/04/063, arXiv:0802.1189.
- [54] M. Cacciari, G. P. Salam, and G. Soyez, “FASTJET user manual”, *Eur. Phys. J. C* **72** (2012) 1896, doi:10.1140/epjc/s10052-012-1896-2, arXiv:1111.6097.
- [55] CMS Collaboration, “Jet energy scale and resolution in the CMS experiment in pp collisions at 8 TeV”, *JINST* **12** (2017) P02014, doi:10.1088/1748-0221/12/02/P02014, arXiv:1607.03663.
- [56] CMS Collaboration, “Performance of missing transverse momentum reconstruction in proton-proton collisions at $\sqrt{s} = 13$ TeV using the CMS detector”, *JINST* **14** (2019) P07004, doi:10.1088/1748-0221/14/07/P07004, arXiv:1903.06078.

- [57] CMS Collaboration, “The CMS trigger system”, *JINST* **12** (2017) P01020, doi:10.1088/1748-0221/12/01/P01020, arXiv:1609.02366.
- [58] CMS Collaboration, “Missing transverse energy performance of the CMS detector”, *JINST* **6** (2011) P09001, doi:10.1088/1748-0221/6/09/P09001, arXiv:1106.5048.
- [59] CMS Collaboration, “Performance of the CMS muon detector and muon reconstruction with proton-proton collisions at $\sqrt{s} = 13$ TeV”, *JINST* **13** (2018) P06015, doi:10.1088/1748-0221/13/06/P06015, arXiv:1804.04528.
- [60] CMS Collaboration, “Performance of the reconstruction and identification of high-momentum muons in proton-proton collisions at $\sqrt{s} = 13$ TeV”, *JINST* **15** (2020) P02027, doi:10.1088/1748-0221/15/02/P02027, arXiv:1912.03516.
- [61] CMS Collaboration, “Jet energy scale and resolution in the CMS experiment in pp collisions at 8 TeV”, *JINST* **12** (2017) P02014, doi:10.1088/1748-0221/12/02/P02014, arXiv:1607.03663.
- [62] CMS Collaboration, “CMS luminosity measurements for the 2016 data-taking period”, CMS Physics Analysis Summary CMS-PAS-LUM-17-001, 2016.
- [63] CMS Collaboration, “CMS luminosity measurements for the 2017 data-taking period at $\sqrt{s} = 13$ TeV”, CMS Physics Analysis Summary CMS-PAS-LUM-17-004, 2017.
- [64] CMS Collaboration, “CMS luminosity measurements for the 2018 data-taking period at $\sqrt{s} = 13$ TeV”, CMS Physics Analysis Summary CMS-PAS-LUM-18-002, 2018.
- [65] T. Junk, “Confidence level computation for combining searches with small statistics”, *Nucl. Instrum. Meth. A* **434** (1999) 435, doi:10.1016/S0168-9002(99)00498-2, arXiv:hep-ex/9902006.
- [66] A. L. Read, “Presentation of search results: the CL_s technique”, *J. Phys. G* **28** (2002) 2693, doi:10.1088/0954-3899/28/10/313.
- [67] The ATLAS Collaboration, The CMS Collaboration, The LHC Higgs Combination Group, “Procedure for the LHC Higgs boson search combination in Summer 2011”, Technical Report CMS-NOTE-2011-005, ATL-PHYS-PUB-2011-11, 2011.
- [68] Y. Gershtein, S. Knapen, and D. Redigolo, “Probing naturally light singlets with a displaced vertex trigger”, *Physics Letters B* **823** (2021) 136758, doi:https://doi.org/10.1016/j.physletb.2021.136758.